Proceedings of the International Conference
Nanomaterials: Applications and Properties
Vol. 4 No 1, 01NNPT05(7pp) (2015)

Visual Detection and Recovery of Mercury in Water and Blood Samples Using Nano-membrane Tubular Architectures

M.A. Shenashen[1], Sherif A. El-Safty[1,2,*]

[1] *National Institute for Materials Science (NIMS), 1-2-1 Sengen, Tsukuba-shi, Ibaraki-ken 305-0047, Japan*
[2] *Graduate School of Advanced Science and Engineering, Waseda University, 3-4-1 Okubo, Shinjuku-Ku, Tokyo, 169-8555, Japan*

(Received 01 June; published online 29 August 2015)

Engineered control over one-dimensional (1D) mesoporous silica nanotubes (NTs) inside anodic alumina membranes (AAMs) has led to various methods for detecting, visualizing, adsorbing, filtering, and recovering ultra-trace concentrations of toxic metal ions, such as Hg2+ and Pb2+, in water and blood. These often "one-pot" screening methods offer advantages over conventional methods in that they do not need sophisticated instruments or laborious sample preparation. This mesoscopic membrane sensor for the naked-eye detection micro-object have large surface area-to-volume ratios and uniformly shaped pores in three-dimensional nanoscale gyroidal structures and its active sites consist of heteroatoms arranged around uniformly shaped pores in three-dimensional (3D) nanoscale gyroidal mesostructures densely coated with the chelating ligand so it permits ultra-fast, specific, pH-dependent visualization and removal of toxic metals at low concentrations from aqueous media, including drinking water and a suspension of red blood cells by means of a colorimetric signal visible to the naked eye, as well as by means of UV–vis reflectance spectroscopy. Removal of target ions from biological fluids was assessed by means of flow cytometric analysis. Our results demonstrate the potential for our membrane sensors to be used for preventing the health risks associated with exposure to toxic metal ions in the environment and blood.

Keywords: Detection**,** Optical Sensor, Mesoscopic Nanotubes, Toxins.

PACS numbers: 87.85.fk, 42.79.Pw

1. INTRODUCTION

The health risks associated with exposure to hazardous inorganic and organic environmental pollutants are a major concern worldwide [1,2]. Heavy metal toxicant such as mercury (Hg^{2+}) is of particular concern because of their adverse physical and neurotoxic effects in most living organisms [2-7]. Indeed, around 400 million tons of Hg^{+2} is commonly detected in air, water, and soil [5-7]. In humans, mercury species, both inorganic (elemental, metallic, or ionic) and organic (e.g., alkyl mercury compounds), negatively affect the nervous, digestive, urinary, respiratory, and immune systems, as well as the skin and eyes. The accumulation of Hg^{2+} in the human body has been shown to result in various cognitive and motor disorders and can cause diseases such as Minamata disease [12-14]. The selective and sensitive detection of toxic heavy metal ions are of great interest because these metal ions cause adverse health and environmental problems [9]. Hg(II) is regarded as the most ubiquitous of these ions because it is highly toxic and has bioaccumulative properties [10]. Hg(II) is highly hazardous because both elemental and ionic mercury can be converted by the bacteria in the environment into methylmercury, which is subsequently bioaccumulated through the food chain. High exposure to Hg(II) affects the brain and its associated functions, resulting in symptoms, such as irritability, nervousness, tremors, vision problems, deafness, and the loss of muscle coordination, sensation, and memory. In addition to the brain, methylmercury damages the kidneys, stomach, heart, and intestines. According to the Environmental Protection Agency guidelines, the concentration of Hg(II) in drinking water must be below 2 μg/L [11].

The natural occurrence of mercury in the environment exposes everyone to very low levels of mercury, but these levels are still lower, and are considered "safe" to breathe. However, mercury becomes toxic at critical dosages. Therefore, the timely and accurately monitoring and measuring trace Hg(II) by developing highly sensitive and selective methods are urgently needed. Even though some powerful analytical methods, such as inductively coupled plasma mass spectrometry, ion selective electrodes, atomic absorption spectrometry, and atomic fluorescence spectroscopy, are being used to monitor low Hg(II) levels [12], they have some drawbacks, such as being time-consuming and expensive, and having low sensitivity, selectivity, and complicated sample preparation processes. To avoid these problems, we followed a different strategy for designing a new method that simultaneously possesses many advantages, such as convenience, simple operation, rapid completion, low consumption, high sensitivity and selectivity, and possible application in field tests and on-site Hg(II) monitoring, especially at harmless levels [13].

Several methods for the detection of heavy metals in biological and environmental samples have been developed, and electrochemical, neutron activation, molecular absorption spectrometry, X-ray fluorescence, atomic absorption spectroscopy, and inductively coupled plasma methods have all been used to identify and quantify toxic metals at the parts-per-billion level (ppb) [14]. However, although these methods are rapid and

* sherif.elsafty@nims.go.jp

extremely sensitive, in practical terms, they require complicated sample preparation techniques, controlled experimental procedures, and well-trained laboratory technicians. Therefore, inexpensive, simple-to-conduct methods that allow the fast response analysis and assessment of the levels of heavy metal ions in environmental and biological samples are needed. In this regard, assessment with the naked eye may be a convenient approach because of its simplicity and efficiency to detect of toxic ions at the safe limits in drinking water [15- 18], and considerable efforts have been made in the development of these sensors.

Nanoscale inorganic materials have received considerable interest in the last two decades owing to uniform and tunable pores as well as stability in organic and inorganic phases, these materials may be used as proper carriers for potential applications. Organic functionalization of these mesoporous inorganic materials in particular has generated considerable attention due to the attractiveness of combining a wide range of organic compound properties with the robust thermal and mechanical stabilities of high-surface-area inorganic solids [19, 20]. Sensors that change colors have the advantages of versatility, ease of use, high sensitivity, low cost, and fast response-time of the chemosensors are induced by receptor "molecular probe"–analyte "cation" interactions [21]. The recent development of optically based chemical sensing platforms has increasingly employed substrates manufactured with advanced processing or fabrication techniques to provide precise control over shape and morphology of the sensor micro- and nanostructure. A study of the effects of particle morphology on the ion selectivity and sensitivity of a solid, nanomaterial-based Cu^{2+} sensor has compared the use of silica nanotubes (NTs) and silica nanoparticles as the sensor platform [22]. Recently, efforts have been made to create novel hierarchical membrane materials. Since Martin's discovery of the one-dimensional nanochannels present in anodic alumina membrane (AAM) [23], several methods have been developed for the incorporation of mesostructure pores of various sizes, shapes, and geometries into the AAM nanochannels [24-27]. Previously, we reported the fabrication of mesoporous silica NTs inside AAM nanochannels by using sol–gel- and aspiration-based methods, which addressed the limitations associated with pre-synthesis methods [25, 28]. Specifically, we were able to 1) achieve the complete, uniform filling of the AAM nanochannels with silica sol–gel precursor without the nanochannel cracking or silica overgrowth, 2) produce hierarchical mesostructures that did not collapse during use in catalysis or separation systems, and 3) prevent gaps from forming between the nanochannel wall and silica composites during high-temperature treatment or after multiple reuse cycles [27,28].

In the present study, we used hierarchical engineering to construct membrane sensor for the detection, filtration and recovery of ultra-trace concentrations of Hg2+ from water and human blood. By using the AAM nanochannels as a scaffold, we fabricated organic colorant-decorated, open-ended NTs within the AAM nanochannels. We then assessed the membrane sensors in terms of recyclability and their ability to detect, and filter Hg2+ in water and human blood. Our findings indicate that our sensor design offers accessibility to the colorant active sites, as evidenced by a detection time that was in the order of seconds. Here, for the first time, we used three simple analysis techniques to examine the detection, filtration, and recovery of Pb2+ and Hg2+ from water and contaminated blood.

2. EXPERIMENTAL

2.1 Materials

All materials were analytical grade and used as purchased without further purification. Tetramethylorthosilicate (TMOS), cetyltrimethyl ammonium bromide [CTAB, $CH_3(CH_2)_{15}(CH_3)_3N^+Br$], N-trimethoxysilylpropylN,N,N-trimethylammonium chloride (TMAC), 2-aminobenzenethiol and carbon disulfide were purchased from Sigma–Aldrich Company Ltd. (USA). Dehydrated pyridine and lead (II), mercury (II) and other metal ion-standard solutions were obtained from Wako Company Ltd. Osaka, Japan. Anodic Alumina Membrane, (AAM) with pore size of 200 nm, diameter of 2.5 cm, and thickness of 60 μm, was purchased from Whatman, Co. Ltd. UK. The commercially available 3-anilino-1-phenylimino-thioure (APIT) probe was used for mercury and purchased from Sigma–Aldrich.

Blood samples were obtained from non-smoking and healthy donors without any pharmacological treatment and occupational exposure to Hg^{2+} ions. Sodium citrate (3.2%, w/v) was used as an anticoagulant at a whole blood ratio of 1:10. Plasma and buffy coat samples were removed after centrifugation of blood for 8 min at 600 rpm. RBC suspensions were washed twice with phosphate buffered saline (PBS). All reagents were used directly upon preparation.

2.2 Fabrication of the membrane sensors

We used hierarchical engineering to fabricate the two membrane sensors used in the present study [25]. First, to create an electrostatic interaction between the silica and the walls of the AAM nanochannels, positively charged islands inside the AAM nanochannels were generated by using N-trimethoxysilylpropylN,N,N-trimethylammonium chloride (TMAC). Anhydrous toluene containing (TMAC) and AAM were refluxed in a Soxhlet apparatus for 24 h under N_2 at room temperature. The mixture was then gently sealed in a round-bottle container, washed with ethanol to remove any unreacted TMAC, and then dried in a vacuum oven at 65 °C . Next, hexagonal mesoporous silica NTs were fabricated inside the AAM by using 1.0 g of cetyltrimethyl ammonium bromide (CTAB), 10 g of ethanol, 2.0 g of tetramethylorthosilicate (TMOS), and 1.25 g of acidified Mill—Q (i.e., H_2O–HCl) water with resistivity of 18.1 MΩ·cm at room temperature. Vacuum-assisted penetration was used to drive the precursor solutions into the membrane channels. The hybrid membrane was then allowed to stand in a sealed container at 45 °C for 10 h until dry. The CTAB surfactant was removed by means of solvent extraction, which avoids the formation of air gaps between the NTs, which are prone to form upon calcination, and then dried at 60 °C. This

produced a thermodynamically stable phase with hexagonal mesoscopic silica NTs inside the AAM nanochannels.

Finally, organic colorants APIT were immobilized on the NTs and protected to maintain electron acceptor and donor strength. Briefly, an ethanoic solution containing the colorant APIT was left without stirring until equilibrium was reached, and then the membrane was washed with deionized water until the probe was no longer eluted. The immobilized APIT colorants into NTs hybrid AAM (i.e., sensor **I**) were used to examine the sensitivity, selectivity and adsorption of Hg^{2+} (Scheme 1). The visible color changes were caused by the pH-dependent coordination of the colorant donor species with the target ions and the subsequent stabilization of the complexes (Scheme 1). The membrane sensor structures and parameters were characterized and determined by using N_2 adsorption-desorption isotherms, small angle X-ray scattering (SAXS), high resolution transmission electron microscopy (HRTEM), scanning transmission electron microscopy (STEM), and dispersive X-ray analysis for elemental mapping (STEM-EDS), field-emission scanning electron microscopy (FE-SEM), and ^{27}Al magic-angle spinning, nuclear magnetic resonance (^{27}Al MAS NMR), respectively (see Supporting Information).

2.3 Material characterizations

Field-emission scanning electron microscopy (FE-SEM) images were obtained (Hitachi S-4300). The insertion into the chamber, the samples were fixed onto the FE-SEM stage using carbon tape before insertion into the chamber. The Pt films were deposited on membrane substrates at room temperature by using an ion-sputter (Hitachi E-1030); the distance between the target and the membrane substrate was 5 cm.

High resolution transmission electron microscopy (HRTEM), scanning transmission electron microscopy (STEM), and dispersive X-ray analysis for elemental mapping (STEM-EDS) were operated at 200 kV electron microscope (JEOL 2000 EX II) which has a point-point resolution of 0.21 nm and a spherical aberration of 0.7 nm. To obtain a cross-sectional TEM image, the calcined mesocage silica NTs hybrid AAM was immersed in a 5 wt% phosphoric acid solution to etch the alumina matrix. The supernatant was collected through the centrifugation. The final solid was then washed several times by Milli-Q water to completely remove excess phosphoric acid and alumina. The MOSs membrane was prepared by dimple grinding followed by Ar ion polishing to record the plan-view TEM image. The TEM images were recorded using a CCD camera. Fourier transform diffractograms (FTD) were recorded by a slow scan charge-coupled device (CCD) camera (Gatan Model 694). All sets of TEM and SEM images of mesoporous silica NTs were recorded after etching of alumina hosts by addition of 5 % H_3PO_4 for 24 h at 25°C.

Small angle X-ray scattering (SAXS) experiments were performed at room temperature. A two-dimensional (2D) confocal mirror (Rigaku Nanoviewer) and a pinhole collimator were used to obtain a focused high-flux/high-transmission and monochromatic X-ray beam of Mo-Kα radiation (λ = 0.07 nm).

The textural surface properties of the mesoporous membrane, including the specific surface area and the pore structure, were determined by N_2 adsorption-desorption isotherms measured using a BELSORP MIN-II analyzer (BEL Inc., Japan) at 77 K. The pore size distribution was determined from the adsorption isotherms by using the Barrett–Joyner–Halenda method. Specific surface area (S_{BET}) was calculated using multi-point adsorption data from a linear segment of the N_2 adsorption isotherms using the Brunauer–Emmett–Teller (BET) theory. Before the N_2 isothermal analysis, all samples were pre-treated at 300 °C for 8 h under vacuum until the pressure had equilibrated to 10^{-3} Torr.

The metal ion concentration was determined using Inductively Coupled Plasma Mass Spectrometry (ICP-MS). The reflectance spectrum of the solid mesocaptor was recorded using a UV-Visible spectrometer (Shimadzu 3150, Japan).

3. RESULTS AND DISCUSSION

3.1 Design of the mesoscopic membrane sensors

We successfully used hierarchical engineering and AAM nanochannels as a scaffold to fabricate mesoscopic membrane sensor. Briefly, the surfaces of the AAM channels were modified to create positively charged islands that would produce an electrostatic interaction between the silica and the walls of the AAM nanochannels. Silica NTs then were fabricated inside the AAM nanochannels by means of direct templating. Finally, the silica NT–AAM hybrid membrane was decorated with the functional colorant 3-anilino-1-phenyliminothioure (APIT; sensor **I**; detecting Hg^{2+}).

3.2 Characterization of the NT–AAM hybrid membrane

We next characterized the NT–AAM hybrid membrane. First, small-angle X-ray scattering profiling of the NT–AAM hybrid membrane showed three scattering peaks in the range $1.7 < q < 4$, which strongly indicated the presence of a hexagonal NT architecture (Figure 1A) [15, 29]. These peaks were assigned to the (100), (110), and (200) planes. The unit cell constants of the bare NTs and the NTs decorated with APIT was 4.7 nm. Although the scattering peaks were broad and of low resolution (Figure 1A), the presence of a mesoscopic architecture implied that the material would be effective as a membrane sensor for the selective chelation of toxic metal ions. N_2 adsorption isotherm analysis provided evidence of the formation of mesoporous NTs throughout the entire length of the AAM nanochannels (Figure 1B). Hysteresis loops H3 indicated the presence of distorted, cylindrical pore openings in the NT–AAM hybrid membrane [30]. The surface area of the hexagonal mesoporous silica NT–AAM hybrid membrane before and after decoration with colorants was approximately 162 $m^2\ g^{-1}$. Surface parameter is a key parameter for increasing the possible applications of AAM as sensors, and captors of toxic pollutants in environmental samples [18]. In addition to the reduction in surface area, pore size and volume were reduced, indicating

that the colorants were successfully immobilized within the NTs.

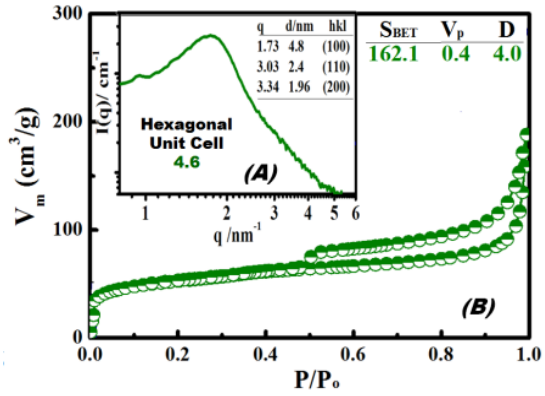

Fig. 1 – (A) SAXS patterns and (B) N_2 adsorption/desorption isotherms at 77 K of the mesoscopic optical membrane sensor **I** (a) before and (b) after the decoration process. The inset (B) shows the surface area (S_{BET}), pore size (D), and pore volume (V_p). The average inter-particle distance d (center to center) can be evaluated from the SAXS peaks using $d = 2\pi/q_{max}$.

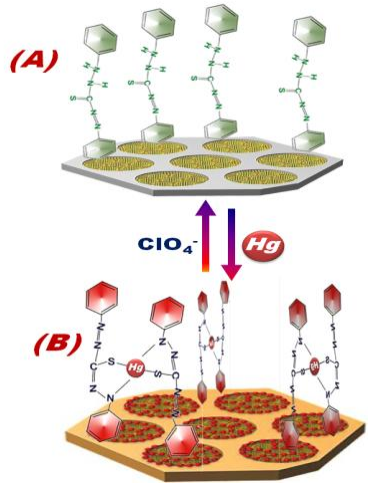

Scheme 1 – Three-dimensional configuration of Sensor I within the NT membrane pores and their complex orientation at specific pH values for Hg^{2+} during the formation of [Hg-(APIT)$_2$] complex.

Field-emission scanning electron microscopy (Figure 2A, B) revealed that the NTs were located within, and aligned parallel to the long axis of the AAM channels. Furthermore, the NTs were seen to be open-ended, which permits fluids to easily access the immobilized colorants [16]. High-resolution transmission electron microscopy (HR-TEM) imaging further confirmed that the mesoporous NTs ran parallel to the wall of the AAM channels and that they had single-strand widths of 70 to 100 nm (Figure 2C, D). TEM images revealed circular, hollow, tubular patterns around the longitudinal axis of the NTs, which appeared in the images as open dots at the edges of the NTs (Figure 2C, D). HR-TEM also revealed a regular band of mesopores (4 nm) at the edges of the NTs. Together the results of this characterization showed that the hierarchical fabrication process resulted in complete, uniform filling of the AAM nanochannels with uniformly aligned, hexagonal, open-ended NTs containing mesoscopic channel-like pores.

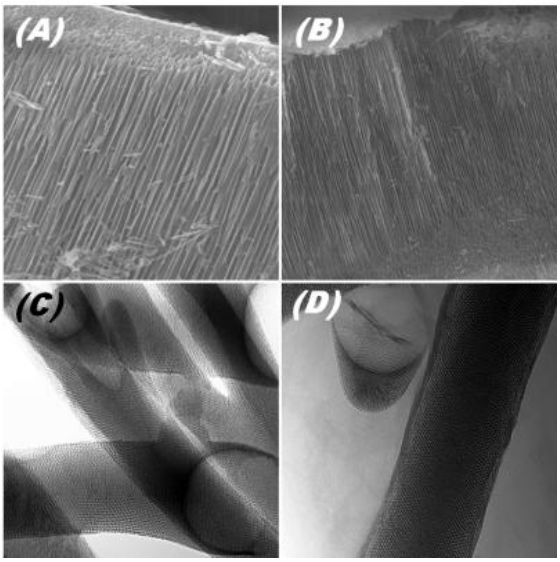

Fig. 2 – (A,B) FE-SEM images of the mesoporous silica NTs hybrid AAM channels synthesized by a template-assisted method of CTAB recorded along the side-view of the mesoporous NT membrane. (C, D) HRTEM images of the silica NTs hybrid AAM channels membrane at different magnifications. Vertical alignment of the silica NTs in the parallel direction along the long axis of the AAM channels; smooth and well-ordered network surfaces over wide-range domains of mesoscopic structures.

Detection, segregation, and filtration of Hg^{2+} from water. We next assessed the suitability of the designed membrane sensors for the detection, segregation, and filtration of Hg^{2+} from water by using a desktop filtration system and a flow-through system [31] The concentration of the metal ions at different points of the experiment was determined by means of inductively coupled plasma mass spectrometry (ICP-MS).

Specificity of the membrane sensors to their target ions. A desktop filtration system was used to examine the specificity of the membrane sensors to their target ions (Figure 3). First, to determine the suitability of the membrane sensors for the selective binding of Hg^{2+} in water, we investigated the tolerance of the sensors to the presence of non-target cations and anions (pH 5; contact time, 2 min; 25 °C). With the addition of individual anions and cations at concentrations 5 to 10 times that of the target ion, no changes in membrane reflectance signaling were observed (Figure 3A). Next we examined the specificity of the sensors to the addition of various groups of cations at concentrations 5 to 10 times that of the target ion. Again, no changes in membrane color visible to the naked eye or reflectance were observed (Figures 3B). Together these results indicated that the presence of non-target ions did not affect the specificity of the Hg^{2+} membrane sensor. This is due that sensors **I** showed a faster, more kinetic (~2 minutes), stronger target-to-colorant binding response than did the non-target ions, and stabilization energy (Scheme 1) of the square-planar [Hg-(APIT)$_2$] complex formed inside nanochannels was high (Figures 3A , B).

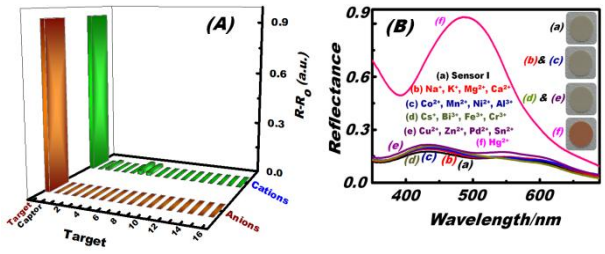

Fig. 3 – Selectivity profiles of the optical membrane sensors I Hg^{2+} ions upon the addition of interference metal ions at optimal sensing conditions. Sequential color and reflectance signaling at λ_{max} values of 485 nm by addition of Hg^{2+} ions particularly at pH 5, to the membrane sensor at 25 °C indicating the response to the membrane sensor (blank, i.e., metal-free assay) and with the addition of interfering cationic species and target Hg^{2+} ions. (A) The quantitative analyses of the spectral reflectance intensity at λ_{max} values of 485 nm of the membrane sensor before (R_o) and after addition of Hg^{2+}ions, and other competitive species (R). (B) Color spectra monitored by addition of Hg^{2+} ions particularly at pH 5, response time of 2 min, and at 25 °C.

To investigate the effect of pH on the ion-detecting capabilities of the membrane sensors, a series of flow-through experiments was conducted at various pH and ion concentrations (Hg^{2+}: 50, 250, and 500 ppb; 25 °C) (Figures 4). At 2 min of contact time, marked changes in the color and reflectance intensity of the membrane sensors were observed, particularly at pH values of 5 indicating that the adsorption of Hg^{2+} by the sensors was pH dependent (Figure 5). We next quantitatively examined the concentrations of Hg^{2+} adsorbed as a function of contact time and pH by using ICP-MS to monitor the concentration of Hg^{2+} ions not adsorbed (permeated) by the membrane sensor (Figures 5A). The results showed that the optimal contact time was approximately 2 min (Figure 5A), and confirmed that pH 5 was optimal in terms of ion-adsorption efficiency (Figure 4B). Furthermore, these results showed that there was a complementary relationship between the amount of target ions adsorbed (rejected) by the membrane sensors and the amount that was not (permeated). Therefore, as the concentration of the target ion in the filtrate (backside) solution decreased, adsorption of the target ion (rejection) by the membrane sensor increased. Together, these adsorption assays showed (1) that the adsorption capacity of the membrane sensors was pH dependent; (2) that the adsorption of the target ions increased with increasing contact time; and (3) that when the pH was 5 of the target ions reached equilibrium at approximately 2 min (Figures 5). The monolayer coverage and adsorption characteristics of Hg^{2+} ions onto the membrane sensor pore surfaces at constant temperature are represented by the Langmuir isotherm based on the following equation; $C_e/q_e = 1/K_l q_m + C_e/q_m$; where q_m (mg/g) is the practical amount of Hg^{2+} ions removed to form the monolayer coverage and K_L is the Langmuir adsorption equilibrium constant (L/mg). Values for adsorption capacity (q_m) and the Langmuir coverage constant (K_L) were obtained from the slope and intercept, respectively, of the linear regions of the Langmuir plots (Figures 6). The q_m values indicated adsorption efficiencies of 94 to 96% for the target ions. Thus, 1.0 g of membrane sensor can theoretically adsorb 0.162 g of Hg^{2+} (at pH 5) from water. Moreover, the K_L values indicated that the adsorption is fully reversible.

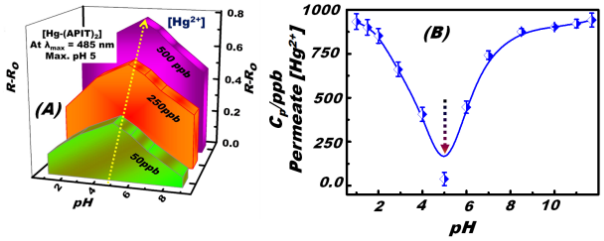

Fig. 4 – pH-dependent response profiles of the Hg^{2+} ions optical membrane sensors. (A) Reflectance spectra of the membrane sensors was obtained at λ_{max} values of 485 nm by addition of different concentrations of Hg^{2+} ions, and at a response time of 2.0 min and at 25 °C. (B) Study the effect of pH values on the rejection/permeation assays of the membrane sensors of 1 ppm Hg^{2+} ion-feed solutions as a function of pH of the feed solution, the Hg^{2+} ions permeated solution was quantitatively measured by ICP-MS. Note: R and R_o represent the signaling reflectance spectra of the membrane sensors at λ_{max} with and without the addition of Hg^{2+} ions.

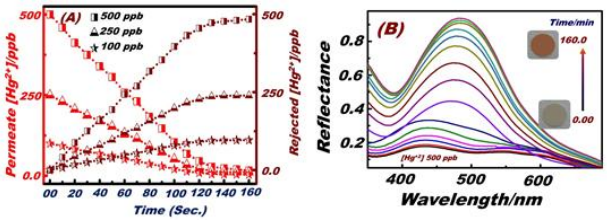

Fig. 5 – (A) Study the effect of contact time of feed solution to membrane sensor II during the rejection/permeation assays of 100, 250, and 500 ppb Hg^{2+} ions feed solution (C_o) at pH 5 and 25 °C. Change in the permeated (C_p) and rejected ($C_R = (C_o - C_p)$ of Hg^{2+} ions onto membrane sensor I with contact time. ICP-MS quantitatively measured the Pb^{2+} ion-rejected/permeated solution. (B) Target ion-time dependence of membrane sensor workability toward 2 ppm Hg^{2+} ions. Sequential color and reflectance signaling responses were monitored as a function of time at pH 5 and at 25 °C.

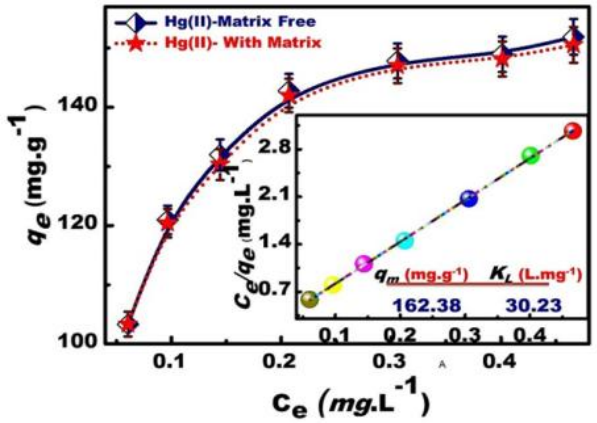

Fig. 6 – A Langmuir adsorption isotherms of the sequestering processes of Hg^{2+} ions from normal (solid-line) and natural (dotted-line), and fitting line was constructed in the linear range of the ion concentration (insets). The relationship was obtained by measuring at pH 5 of Hg^{2+} ions, contact time of 2 min and at 25 °C using the optical membrane sensor.

Recyclability is a key principle in the sensor and adsorbent field; therefore, we next investigated the recyclability of our developed membrane sensors by

subjecting them to multiple reuse cycles. To remove adsorbed target ions, we vacuum-filtered stripping agents through the sensors (0.02 M $HClO_4$ for Hg^{2+} ions,). After eight reuse cycles, a minimal decrease in reflectance was observed, which represents a slight decrease in adsorption efficiency (Figure 7). However, this decrease in rejection "adsorption" efficiency (R_E %) had little effect on the overall efficiency of the membrane sensors. The recyclability of the membrane sensors indicates that the stripping agents were able to decomplex the target ions from the sensor. It is possible that the reduction in efficiency was a result of the recycling process, where treatment with the stripping agents removed a small amount of the colorant from the membrane sensor surface each time, leading to a proportional decrease in adsorption. However, the detection, removal and recovery worktability of Hg^{2+} ion membrane sensors were retained up to twenty times of reuse/cycles. Then, the reused membrane sensors were washed with ethanol for 24 hrs. to release the ligand dressing the tubular-structured cavity and to reopen the pore channels for further fabrication of sensor layouts [32,33]. Our findings also indicate that toxicity control of Pb^{2+} and Hg^{2+} ions during elution and producing membrane filters with high fidelity would reduce the amount of waste produced.

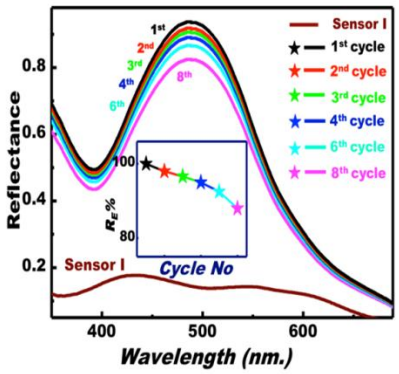

Fig. 7 – (A) Reflectance spectra of mesoscopic membrane sensor during the optical sensing/filtration efficiency of the 0.5 ppm Hg^{2+} ions with reuse cycles at pH 5, and at 25 °C. (inset) the rejection efficiency ((R_E%= (C_o-C_p/C_o) x100)) of the mesoscopic optical membrane sensor for toxic Hg^{2+} ions after eight sensing/filtration reuse/cycles. The experiments were performed at 25 °C, pH 5 for Hg^{2+}, with the overall volume maintained at 20 mL, concentration of metal is 1 ppm and sensing signal responses were obtained after contact time of 2 min. Note: the C_p and C_o were determined by ICP-MS; however, the reflectance spectra indicating the color change of the membrane sensors after rejection of metal ions were monitored by UV–visible spectroscopy.

Detection and removal of Pb^{2+} and Hg^{2+} in human blood. Early diagnosis and monitoring of lead and mercury poisoning is important for the protection of human and animal health, particularly in developing countries.[4] Blood samples provide complete information on heavy metal exposure; [6] therefore, methods for the detection and removal of Hg^{2+} in contaminated blood are needed urgently.

To evaluate the efficiency of our membrane sensors for removing toxic metals from blood, we used a hemolysis assay (Figures 8). Briefly, Hg^{2+} (5 μM) ions were added to a suspension of RBCs. One of the membrane filters was then added and the mixture incubated for 12 h to ensure complete inhibition of the toxicity induced by the metal ions. Metal ion-mediated hemolysis of the RBCs and release of hemoglobin was markedly reduced by the addition of the membrane sensors (Figures 8), indicating that these membrane sensors could be useful for reducing the toxicity associated with exposure to Hg^{2+} [33].

In this experimental assay, when the Ptd-L-Ser receptor was exposed to the outer surface of the RBC membrane for 12 h in the presence of 0.3 μM of Hg^{2+}, the addition of Annexin-V-Fluos indicator to the RBCs resulted in the production of green fluorescence caused by the interaction of the Annexin-V-Fluos with the Ptd-L-Ser receptors on the RBC membrane. The addition of toxic ions indices RBC toxicity, stimulates the Ptd-L-Ser receptor of RBC surface, and creates the green fluorescence, as a result of indicator-to-receptor binding [8, 33]. Furthermore, these interactions were measured by means of flow cytometric analysis (Icyte-Sony). The percentages of annexin-binding cells and mean fluorescence intensity were used as indicators of metal ion-induced toxicity in RBCs (Figure 8).

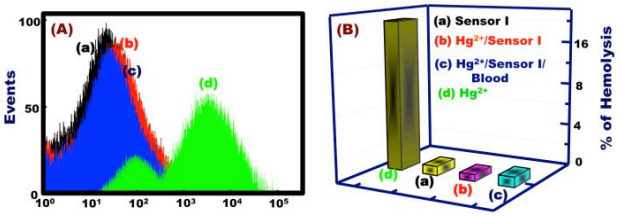

Fig. 8 – (A) Histogram of annexin binding RBCs incubated for 24 h in presence of 100 μM H_2O_2 (a) sensor I, (b) 1 μmol L^{-1} Hg^{2+}/sensor I membrane, (c) 1 μmol L^{-1} Hg^{2+}/sensor I membrane/Blood and (d) 1 μmol L^{-1} Hg^{2+}. (B) Hemolysis assay resulting from the incubation of 3 μmol L^{-1} Hg^{2+} using RBC suspension, and hemolysis inhibition due to the removal of Hg^{2+} by the sensor I.

4. CONCLUSIONS

Toxic metals in the environment are a serious concern because of increasing urbanization and industrialization. The serious health problems caused by toxic metal ions such as Hg^{2+} are of particular concern because of their persistence in the environment. Therefore, improved methods for the selective detection and removal of toxic metal ions from biological and environmental samples are urgently needed. In the present study, we developed mesoscopic membrane sensor for the detection, filtration and recovery of Hg^{2+}. The solid-state, ion-detecting sensor was characterized by a large surface area-to-volume ratio and a uniform arrangement of mesoscopic pores that contained immobilized organic colorant that changed color and allowed the naked-eye detection and removal of trace concentrations (ppb) of Hg^{2+} from water and blood. Our results showed that pH and contact time were key factors that affected the selectivity and sensitivity of the fabricated membrane sensors. We also showed that these membrane sensors were effective at removing Hg^{2+} from human blood, and therefore these sensors may have valuable medical applications.

REFERENCES

1. A. Afal, S.W. Wiener, *Metal toxicity*, *Medscape.org,* **2014**-04-21.
2. A.S. El-Safty, M. Ismael, A. Shahat, M.A. Shenashen, *Envir. Sci. Poll. Res.* **20**, 3863 (2013).
3. R. Dufault, B. LeBlanc, R. Schnoll, *Environ. Health* **8**, 2 (2009).
4. H. Needleman, *Ann. Rev. Med.* **55**, 209 (2004).
5. A. S. El-Safty, M.A. Shenashen, *TrAC Trend Anal. Chem.* **48**, 98(2012).
6. J.H. Jung, J.H. Lee, S. Shinkai, *Chem. Soc. Rev.* **40**, 4464 (2011).
7. World Health Organization 2013. *Stop lead poisoning in children.* Viewed **2014**-05-17 17.
8. S. El-Safty, M.A. Shenashen, *Anal. Chim. Acta* **694**, 151 (2011).
9. a) H.T. Bessbousse,T. Rhlalou, J.-F. Verchere, L. Lebrun, *J. Membrane Sci.* **325**, 997 (2008) b) S.A. El-Safty, A. Ismail, T. Matsunaga, F. Mizukami, *Chem. Eur. J.* **13**, 9245 (2007). c) T. Balaji,; S.A. El-Safty, H. Matsunaga, T. Hanaoka, F. Muzukami, *Angew. Chem.* **45**, 7260 (2006), d)A. Renzoni; F. Zino, E. Franchi, *Environ. Res.* **77**, 68 (1998).
10. a) J.V. Ros-Lis, M.D. Marcos, R. Mártinez-Mánez, K. Rurack, J. Soto, *Angew. Chem.* **44**, 4405 (2005), b) L. Nicole, C. Boissiere, D. Grosso, A. Quach, C. Sanchez, *J. Mater. Chem.* **15**, 4405 (2005).
11. World Health Organization (WHO), Background document for development of WHO Guidelines for Drinking-water Quality, *Mercury in Drinking-water*, WHO/SDE/WSH/05.08/10 (**2005**).
12. a) K. Chen, G. Lu, J. Chang, S. Mao, Y. Yu, S. Cui, J. Chen, *Anal. Chem.* **84**, 4057 (2012). b) F. Zahir, J.S. Rizwi, K.S. Haq, R.H. Khan, *Environ. Toxicol. Pharmacol.* **20**, 351 (2005).
13. a) K. Leopold, M. Foulkes, P. Worsfold, *Anal. Chim. Acta*, **663**, 127 (2010), b) R.K. Mahajan, I. Kaur, T.S. Lobana, *Talanta* **59**, 101 (2003). c), R. Puk, J.H. Weber, *Anal. Chim. Acta* **292**, 175 (1994). d) N. Ahalya, T.V. Ramachandra, R.D. Kanamadi, *J. Chem. & Enviro. Res.* **7**, 71 (2003), (e) J. Aguado, J.M. Arsuaga, A. Arencibia, *J. Hazard. Mater.* **163**, 213 (2009).
14. B.B. Kebbekus, *In sample preparations techniques in analytical chemistry* (Eds: S. Mitra), (Jonh Wiley and Sons: Inc., New Jersey 2003).
15. J.V. Ros-Lis, R. Casasús, M. Comes, C. Coll, M. Marcos, R. Martínez-Máñez, F. Sancenón, J. Soto, P. Amorós, J. El Haskouri, N. Garró, K. Rurack, *Chem. Eur. J.* **14**, 8267 (2008).
16. S. Jiang, R. Cheng, R. Ng, Y. Huang, X. Duan, *Nano Research* **8**, 257 (2015).
17. J. Duan, L. Song, J. Zhan, *Nano Research* **2**, (2009).
18. M.A. Shenashen, E.A. Elshehy, S.A. El-Safty, M. Khairy, *Sep. Pur. Tech.* **116**, 73 (2013).
19. A.S. El-Safty, M.A. Shenashen, M. Khairy, M. Ismeal, *Chem. Commun.* **48**, 6708 (2012).
20. A.S. El-Safty, M.A. Shenashen, M. Khairy, M. Ismeal, *Adv. Funct. Mater.* **22**, 3013 (2012).
21. A.S. El-Safty, M.A. Mekawy, A. Yamaguchi, A. Shahat, K. Ogawa, *Chem. Commun.* **46**, 3917 (2010).
22. S.J. Lee, D.R. Bae, W.S. Han, S.S. Lee, J.H. Jung, *Eur. J. Inorg. Chem.***10**, 1559 (2008).
23. C.R. Martin, *Science* **266**, 1961 (1994).
24. A.S. El-Safty, M.A. Mekawy, A. Yamaguchi, A. Shahat, K. Ogawa, N. Teramae, *Chem. Commun.* **46**, 3917 (2010).
25. A.S. El-Safty, *TrAC Trends Anal. Chem.* **30**, 447 (2011).
26. D.Y. Kang, J. Zang, E.R. Wright, A.L. McCanna, C.W. Jones, S. Nair, *ACS Nano* **8**, 4897 (2010).
27. S. Meoto, M-O Coppens, *J. Mater. Chem. A.* **2**, 5640 (2014).
28. A.S El-Safty, A. Shahat, W. Warkocki, M. Ohnuma, *Small* **7**, 62 (2011).
29. B. Platschek, N. Petkov, T. Bein, *Angew. Chem.* **45**, 1134 (2006).
30. a) S. Pikus, L.A. Solovyov, M. Kozak, M. Jaroniec, *Appl. Surf. Sci.* **253**, 5682 (2007), b) S.A. El-Safty, D. Prabhakaran, Y. Kiyozumi, F. Mizukami, *Adv. Funct. Mater.* **18**, 1739 (2008).
31. a) A.S. El-Safty, M.A. Shenashen, A. Shahat, *Small* **9**, 2288 (2013), b) M.A. Shenashen, A.S. El-Safty, E.A. Elshehy, E. *Analyst* **139**, 6393 (2014), c) A.S. El-Safty, E.A. Elshehy, M. Khairy, *Eur. J. Inorg. Chem.* **1**, 179 (2015), d) M. Khairy, S.A. El-Safty, M.A. Shenashen, *TrAC Trends Anal. Chem.* **62**, 56 (2014).
32. a) A.S. El-Safty, A.A. Ismail, H. Matsunaga, T. Hanaoka, F. Mizukami, *Adv. Funct. Mater.* **18**, 1485 (2008), b) M.A. Shenashen, S.A. El-Safty, E.A. Elshehy. *J. Hazard. Mater.* **260**, 833(2013).
33. A.S. El-Safty, M.A. Shenashen, *Sens. Actuat. B: Chem.* **183**, 58 (2013).